Experimental analysis of carbon-based Phase Change Materials composites for a fast numerical design of cold energy storage systems

Applied Thermal Engineering 231 (2023) 120907

Contents lists available at ScienceDirect

Applied Thermal Engineering

journal homepage: www.elsevier.com/locate/ate

Experimental analysis of carbon-based Phase Change Materials composites for a fast numerical design of cold energy storage systems

Alessandro Ribezzo [a], Luca Bergamasco [a], Matteo Morciano [a], Matteo Fasano [a], Luigi Mongibello [b], Eliodoro Chiavazzo [a,*]

[a] Department of Energy, Politecnico di Torino, Corso Duca degli Abruzzi 24, 10129 Torino, Italy
[b] Enea Portici, P.le Enrico Fermi, 1 - Località Granatello, 80055 Portici (Na), Italy

ARTICLE INFO

Keywords:
Thermal energy storage
Phase change materials
Nanocomposite
Thermal conductivity enhancement
Thermal interface resistance

ABSTRACT

The adoption of highly conductive nanofillers within a phase change material (PCM) matrix is considered a promising solution to enhance the effective thermal conductivity of the resulting nanocomposite, thus possibly increasing specific power and energy density in latent thermal energy storage plants. However, the expected significant property enhancement of such composite materials is often unmet, with one of the key reason being the critical and poorly studied role played by too high thermal resistances at the nanofiller-matrix interfaces limiting the heat flux within the material. One of the contributions of this work is providing an estimate of the value for such resistances in relevant cases for cold energy storage found to be in the range of: $3 \cdot 10^{-7}$ - $3 \cdot 10^{-6}$ [m^2K/W]. Those estimates have been obtained by exploiting a synergistic study combining a numerical analysis, based on mean-field theory calculations and finite element simulations, with experimental assessment of the resulting properties of nanocomposite samples. In addition, we show how the numerically predicted values of the effective thermal conductivity can be used as input data in an approximated numerical analysis of a lab-scale shell & tube storage tank connected to a daily domestic user, adopted for the storage of sub-ambient temperature thermal energy. This leads to a novel multi-scale analysis coupling the material effective properties and the expected behavior at the plant level, thus allowing a preliminary computationally efficient optimization of the storage system under analysis. Compared to computational fluid dynamics simulations, the approximated design approach proved to predict the propagation front up to 30% accuracy.

1. Introduction

To reach the targets of the Paris Agreement on climate change, renewable energies are expected to achieve a sixfold growth by 2050, providing more than 60% of the global power. A two-fold growth of the global Thermal Energy Storage (TES) capacity for cooling applications is required to comply with the expected demand in the next decade [1]. The increasing development of technologies for the conversion of renewable energy sources, such as solar energy, is indeed increasing the necessity to store and manage thermal energy efficiently [2]. Renewable energy sources, in fact, are characterized by their intrinsic discontinuous and intermittent nature [3]; as such, the availability of energy storage technologies becomes crucial for their efficient exploitation.

Among TES technologies [4–6], those based on Phase Change Materials (PCMs) currently represent one of the most promising solutions, thanks to a sufficient technological maturity [7]. PCMs, indeed, can provide higher energy density as compared to traditional technologies based on sensible heat storage; however, their low thermal conductivity may imply incomplete phase transitions in storage plants and thus modest power densities and significantly reduced effective energy capacities [8]. PCM composites, resulting from the dispersion of highly conductive nano- or micro-fillers in a bulk PCM matrix, show promising potential to overcome the above limits thanks to an important enhancement in thermal conductivity with a marginal reduction of latent heat [9–14]. Carbon-based nanofillers such as carbon nanotubes (CNTs) [15], carbon nanofibers (CNFs), and graphene nanoplatelets (GNPs) are among the most frequently adopted materials, due to their outstanding mechanical and thermal properties [16–18].

The measured effective thermal conductivity of PCM nanocomposites is often below the theoretical expectations, such as that predicted by percolation theory or effective medium theory [19,20]. One reason, among others, for such a partial success stands in the thermal resistances at the interfaces between the nanofillers and the matrix [21]. As a matter of fact, thermal resistances limit the heat flux within the

* Corresponding author.
E-mail address: eliodoro.chiavazzo@polito.it (E. Chiavazzo).

https://doi.org/10.1016/j.applthermaleng.2023.120907
Received 20 July 2022; Received in revised form 29 March 2023; Accepted 8 June 2023
Available online 13 June 2023

material and cause a non-linear dependence of the effective thermal conductivity with the content of the nanofiller [22,23]. Accurate estimates of the value of such resistances are particularly challenging, due to the high complexity of the underlying phenomena. Thermal interface resistances depend on the chemical and physical nature of the matrix and the nanofillers, on the geometry of nanofillers and on their dispersion within the matrix. Consequently, the preparation procedure for the production of these nanocomposites can affect their thermo-physical properties [24]. Most studies in the field of polymeric-based [25,26] and PCM-based nanocomposites [27], have adopted interfacial thermal resistance values that were previously predicted by molecular dynamics simulations [19]. However, the latter are not able to assess the impact of the factors that occur at scales bigger than the nanoscopic one. To the authors knowledge, the estimate of the interfacial thermal resistances obtained by comparing experimental measurements and numerical simulations in nanocomposites has not been extensively treated in literature [28], especially in the field of PCM nanocomposites.

One of the main aims of this work is to characterize the values of the thermal interface resistances as a function of the nanofiller content for PCM nanocomposites, filled with different carbon-based fillers. To this, we compare experimental measurements with finite element (FE) simulations. In particular, we focus on PCM nanocomposites obtained by dispersing three distinct Graphene Nano Platelets (GNPs), with different characteristic sizes, within a bio-based PCM [29]. FE simulations are performed based on the implementation of the modified thermal conductivity model proposed by Chu et al. [25], which takes into account the role of the thermal interface resistances. Subsequently, the thermal interface resistances values were included in Mean Field (MF) theory calculations, thus obtaining the effective thermal conductivity as a function of the nanofiller content in a wider nanofiller content range than the experimentally measured one.

Finally, the effective thermal properties of the nanocomposites, including the thermal conductivity, were used as input data for the numerical analysis of a lab-scale application. The chosen application consists of a shell & tube tank, connected to a daily domestic user aimed at the storage of cooling energy. The aim of this analysis was the development of a new fast procedure for the thermal design of PCM-based storage systems, thus not relying on time-expensive CFD simulations. In this context, the above analysis is based on a one-dimensional solution to the Stefan problem [30], which was properly modified to take into account the variation of the boundary conditions (temperature variation of heat transfer fluid) that were experimentally tested. The output of this analysis was to define two thresholds of the nanofiller content: the minimum content, i.e. the content at which complete transition is expected to occur within the tank during the charging and discharging processes, and the optimal content (in the spirit of a Pareto perspective), representing the best compromise between specific energy and specific power. A comparison between the analytical approach proposed in this work and CFD simulations for the solidification of the bulk PCM was also carried out to verify the analytical model proposed in this work.

The outline of the paper is as follows: in Section 2, the materials and experimental setup exploited for the thermal conductivity measurements and the plant analysis are described; the theoretical framework of the material and plant scale analysis is reported in Section 3; in Section 4 the results of the experimental and numerical analysis for both scales are presented and discussed; finally, in Section 5 the overview of the work is reported and some future possible improvements proposed.

2. Materials and methods

2.1. Material analysis

The adopted bio-based PCM matrix (with commercial name *PureTemp PT15*) has a nominal melting point of 15 °C [31]. Three GNPs were used as nanofillers: GNP25 (*xGnP M-25*, Merck KGaA), GNP15 (*xGnP M-15*, Merck KGaA), and GNP5 (*xGnP M-5*, Merck KGaA). The GNPs were provided as powders by the supplier. Among the fillers characterized by outstanding thermal properties (as carbon nanotubes [32] and carbon nanofibers [33]), GNPs were selected on the basis of their easiness of dispersion during mixing processes and their two-dimensional structure, which leads to remarkable thermal conductivity enhancements [33,34]. Table 1 summarizes the geometrical properties of the nanofillers and all the PCM nanocomposites experimentally tested. Here, the Aspect Ratio (AR) is defined as the ratio between the lateral size and the thickness of the nanofiller, while the weight content was computed as the ratio between the weight of the additives and the total weight of the composite.

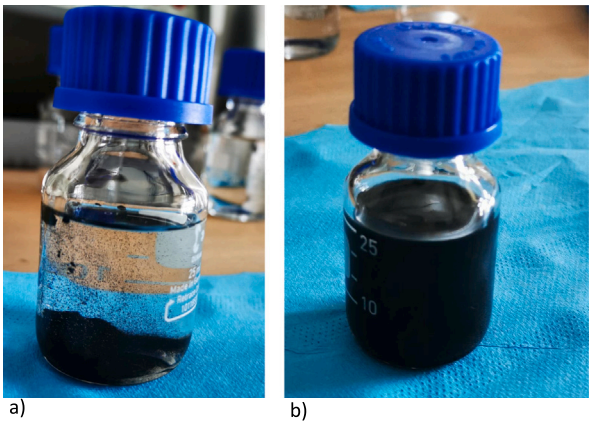

Fig. 1. Sample containing the PCM and nanofillers (a) before and (b) after the mixing process.

Initially, the PCM (in liquid phase at room temperature) and the GNPs were inserted in a sealed glass test tube of ~ 25 ml and weighted by means of a balance (*220/C/2*, Radwag) with a precision of 0.1 mg. The PCM nanocomposites were prepared by mixing the filler (GNP25, GNP15 or GNP5) and the PCM following a two-step procedure, consistently with those reported in the literature [35–37]. First, a preliminary mixing (10 min) was performed by a magnetic stirrer (*AG20D*, OrmaEurotek). Afterward, the sample was further mixed for 20 min using an ultrasonicator (*GTSONIC-GT3*, OrmaEurotek) to obtain a homogeneous dispersion. In Fig. 1 the sample before (a) and after (b) the mixing process is shown. The thermal conductivity of PCM nanocomposite in the liquid phase was first measured (at room temperature) by pouring ~ 1 ml of sample into a mold in contact with the thermal conductivity sensor. The measurement was performed by a thermal conductivity analyzer (*TCi*, C-Therm Technologies Ltd.), which is based on a modified transient plane source. This modified technique presents solely a single-side interface for the measurement of the thermal conductivity, contrarily to the double-sided interface exploited in the traditional transient plane source [38]. In Fig. 2, the PCM nanocomposite within the mold of the sensor is shown. The sensor, still in contact with the nanocomposite, was then placed inside a thermostated chamber (*Tenney TPS junior*, Tenney Environmental) regulated at a fixed temperature of 5 °C. The thermal conductivity of the PCM nanocomposite sample was secondly measured for the solid phase. Finally, the sensor was cleaned and heated up to ambient temperature. Meanwhile, additional GNP was added to the glass sample (Fig. 1), thus repeating the procedure. Three samples containing PT15 and different weight content of GNP15 are represented in Fig. 3.

Table 2 summarizes the thermophysical properties of the PCM and the nanofillers tested.

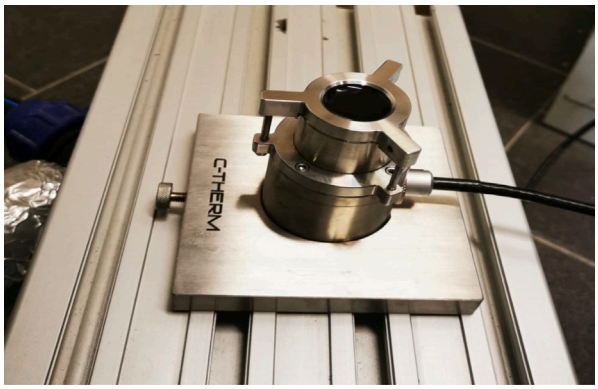

Fig. 2. Image of the thermal conductivity sensor. The nanocomposite in the liquid phase (black material) is inside the mold (upper part of the sensor). The cylindrical part at the bottom is the sensor, which measures the thermal conductivity.

Table 1
Overview of the additives type, their lateral size (d), thickness (t), aspect ratio (AR), and weight content of the thermal conductivity measurements performed. L and S indicate if the measurements of the effective thermal conductivity of the nanocomposite in liquid and solid phases were performed, respectively.

Filler	d [μm]	t [nm]	AR [-]	Content [%]	Meas.
GNP25	25	7	3571	0.266	L-S
				0.619	L-S
				1.36	L-S
				3.53	L
GNP15	15	7	2142	0.132	L-S
				0.533	L-S
				1.11	L-S
				2.92	L
GNP5	5	7	714	0.213	L-S
				0.808	L-S
				1.79	L-S
				2.68	L

Table 2
Thermophysical properties of the materials used in this study. Values inside the brackets refer to the liquid phase of the PCM. * The thermal conductivity in the radial direction of the GNP is reported.

		Materials	
		PCM	GNP
Properties	ρ [kg/m^3]	950 (860)	2100 [39]
	λ [W/mK]	0.247 (0.155)	3000* [35]
	L [J/kg]	182e3	–
	c_p [J/kgK]	2250 (2560)	1200 [39]

2.2. Plant analysis

Concerning the plant analysis, Fig. 4 shows the considered plant, which is composed of the chiller (*ThermoFlex24000*, Thermo Scientific), the heat exchangers used for the experimental assessment of the user cooling load, and the TES tank. The simulated user was a single-family house, characterized by a surface area equal to 150 m^2 and an envelope shape factor of 0.9 m^{-1}, located in the Italian climatic zone E. The yearly thermal energy demand and the daily thermal and electrical load profiles for air conditioning in the warm season have been evaluated as by Mongibello et al. [40]. In Fig. 5, the hourly averaged cooling load profile of the considered user for a standard day is depicted.

The shell & tube tank containing the PCM (Fig. 4) was produced in Plexiglas, with and without thermal insulation. The tank was composed of: a tube bundle with 66 stainless steel 3/8" pipes; stainless steel bottom (inflow) plenum; stainless steel upper (outflow) plenum with vent valve; transparent shell with an internal diameter equal to 500 mm and a thickness of 5 mm. The shell & tube configuration is particularly suitable for latent heat thermal energy storage (LHTES) for three main reasons: (i) it allows to realize indirect cooling energy storage by separating the heat transfer fluid and the storage material; (ii) such a configuration allows to obtain a uniform heat transfer along the cross sections of the tank and a relatively high total heat transfer surface; (iii) it represents an already available commercial solution that can be easily customized by the shell & tube heat exchanger manufacturers themselves. Indeed, most of the applications with stand-alone LHTES found in the specific literature adopt shell & tube tanks [41–45].

In the plant considered, therefore, for the given mass flow rate $\dot{m}_{HTF}$ and chiller setpoint temperature $T_{chiller,out}$, the charge and discharge of LHTES depend on the PCM characteristics and heat load of the user. If the user cooling energy load is relatively low and the water temperature at the exit of the user $T_{tank,in}$ is lower than the PCM solidification temperature T_m, the discharging of the storage tank occurs. On the other hand, the storage system is charged when the user cooling energy load is relatively high and $T_{tank,in}$ is higher than T_m. Such a layout and operation strategy allows to limit the variation range of the chiller inflow temperature (which is equal to that at the outlet of the tank $T_{tank,out}$, by neglecting the heat losses within the pipes), thus reducing its maximum absorbed power. Demineralized water was adopted as heat transfer fluid within the tubes. It is worth noting that, although the aim of the plant is cold energy storage, the terminology of the charging and discharging phases is used according to the literature convention, i.e. the charging phase occurs when the heat is absorbed by the PCM.

3. Theoretical framework

3.1. Material analysis

The numerical model developed to compute the effective thermal conductivity of the PCM nanocomposites was based on FE simulations and MF theory calculations, both performed by means of the Digimat software [46].

Digimat-MF performs a semi-analytic mean-field homogenization to compute the effective thermal conductivity of a nanocomposite as a function of its microstructure and material properties. The software relies on a Representative Volume Element (RVE) of the material, which contains the geometrical information (size, orientation and position) of the nanofillers. Digimat-MF exploits the mean-field homogenization proposed by Mori and Tananka [47] (based on an approximation of the Eshelby solution [48]), which models the behavior of each inclusion as isolated within the matrix. This approximation is particularly suitable for nanocomposites with low filler content (< 20% in volume) [46]. The orientation of each nanoinclusion is described by a versor, which is a function of two spherical angles. In the case of RVE containing 3D-oriented nanofillers, a two-step homogenization is performed. First, the initial RVE (I) is substituted by an equivalent RVE (II), where the nanoinclusions with the same orientation are merged into pseudo-grains. Each pseudo-grain has a specific orientation and a nanoinclusion content; therefore, it is homogenized following the Mori and Tananka model in RVE (III) [47]. Finally, the pseudo-grains are further homogenized by means of the Voigt model [49], obtaining an equivalent homogenized component in RVE (IV). The procedure is schematically shown in Fig. 6.

The FE simulations were performed by means of Digimat-FE, which exploits an RVE similar to that of Digimat-MF. This RVE has a cubic shape with an edge length of some μm, depending on the nanofiller type and weight content. Upon meshing of the RVE, a heat flux between parallel faces of the RVE is imposed. Hence, the thermal conductivity is computed by imposing Fourier's law $\boldsymbol{\phi} = -\lambda_i \nabla T$, where $\boldsymbol{\phi}$ is the heat flux, λ_i the thermal conductivity along the ith direction and T the

Fig. 3. Samples of PT15 additivated with (a) 0.132%, (b) 0.533% and (c) 1.11% in weight content of GNP15. In (b) and (c), the darker portion of the material at the bottom is due to the partial precipitation of the nanofillers.

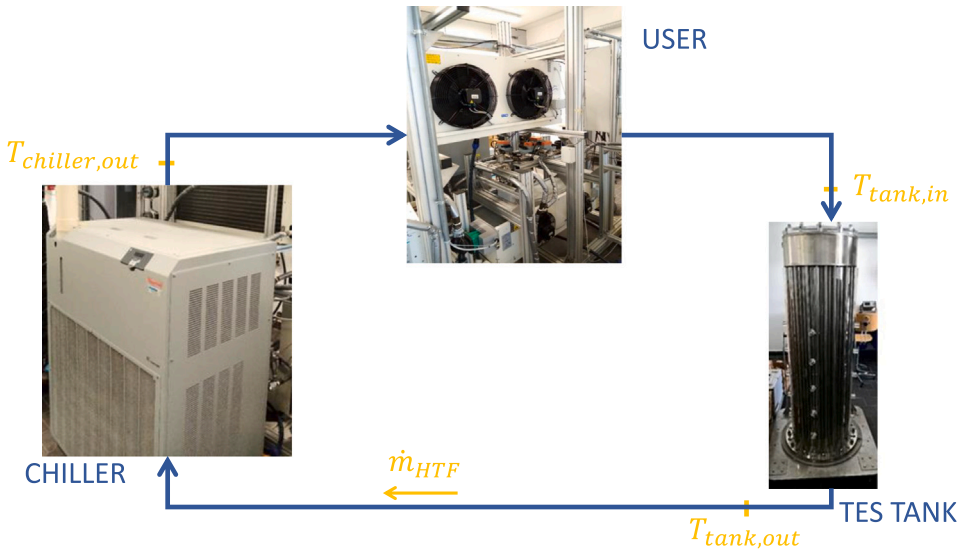

Fig. 4. Schematic representation of the considered plant, which is composed of the TES tank, the chiller and the user (which was simulated by means of the heat exchanger). The main figures of merit of the heat transfer fluid are also depicted: the mass flow rate $\dot{m}_{HTF}$, and the temperatures at the inlet of the tank $T_{tank,in}$, at the outlet of the tank $T_{tank,out}$ and at the outlet of the chiller $T_{chiller,out}$.

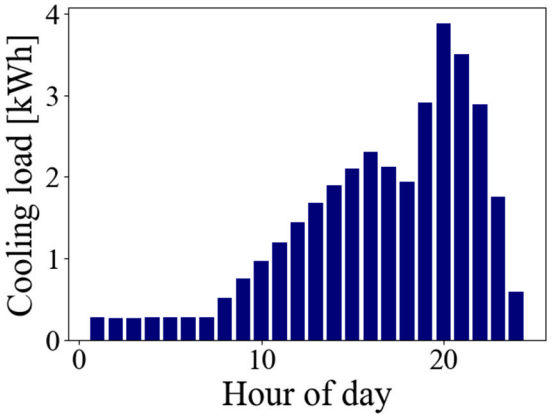

Fig. 5. Hourly averaged thermal load profile of the user.

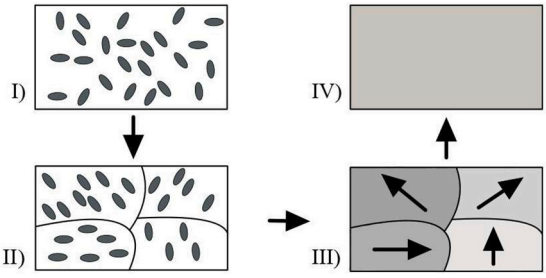

Fig. 6. Homogenization procedure performed by Digimat-MF to obtain a homogeneous equivalent RVE.

temperature. The overall thermal conductivity of the PCM nanocomposites is obtained as the average of the effective thermal conductivity components computed in the three directions. A periodic geometry was imposed along the three coordinates, as the RVE is expected to represent a random portion of the composite material. An internal FE solver, based on the CASI iterative solver type, was used for the FE simulations [46].

First, preliminary MF theory calculations were performed to define the impact of the Aspect Ratio (AR), i.e. the ratio between the diameter and the thickness of nanofiller, on the effective thermal conductivity. Fig. 8 shows the obtained effective thermal conductivity of the nanocomposite as a function of the aspect ratio. It is found that the simulation points can be conveniently fitted imposing a logarithmic behavior as a function of the AR. Interestingly, we notice that similar results were obtained by experimental measurements performed by Depaifve et al. [50] and by numerical simulations carried out by Yang et al. [51]. This preliminary analysis allowed us to perform the FE simulations using RVEs with nanofillers at moderate values of the AR. The reason of this choice was the difficulty of the software in simulating

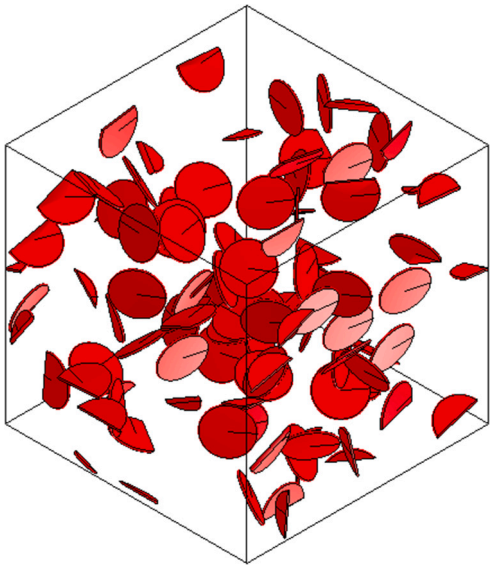

Fig. 7. Example of the RVE exploited for the FE simulations. The white portion within the cube represents the PCM and the red one the simulated GNPs. The specific RVE contains 2.92% in weight content of GNP15, with a simulated AR of 25.

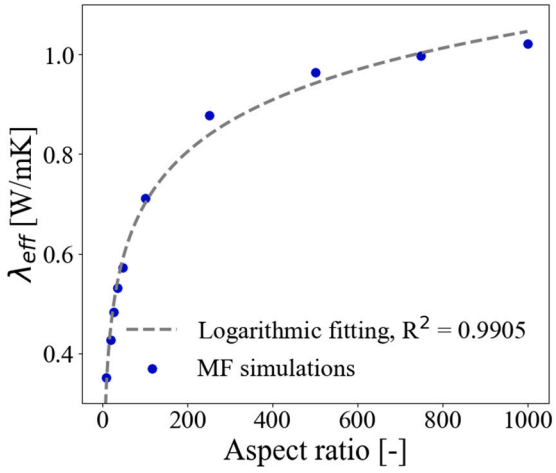

Fig. 8. Effective thermal conductivity (λ_{eff}) computed by MF theory calculations as a function of nanofiller AR (blue dots). The dashed gray line is the logarithmic fitting.

nanofillers with large ARs. In fact, FE simulations of RVE containing nanofillers with real ARs would have required a meshing complexity beyond the possibility of the software. Consistently, the subsequent FE simulations were performed considering GNPs at three different reduced AR (25, 40 and 50). An example RVE is shown in Fig. 7. On the basis of the above observation, a logarithmic extrapolation was adopted to compute the effective thermal conductivity of the nanocomposite with nanofillers at the desired aspect ratio. This procedure has been previously validated against experimental measurements and literature data [52].

Then, a synergistic approach between FE simulations and experimental measurements was followed to estimate the overall value of thermal resistances at interfaces in the nanocomposite material. To this end, a sensitivity analysis of the numerical simulations with respect to the thermal interface resistance value was compared with experimental measurements, thus obtaining estimated values of the thermal interface resistances as a function of nanofiller type and content. The overall thermal interface resistance R_{ck} is considered to take into account both the contacts between nanofillers and matrix and between

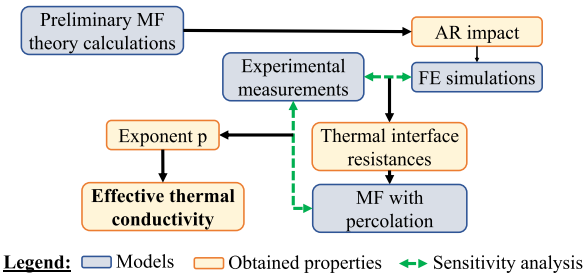

Fig. 9. Schematic representation of the various tools exploited and properties obtained to estimate the effective thermal conductivity of the phase change nanocomposites.

the nanofillers themselves. When dealing with thermal interface resistances, a key property to consider is the percolation threshold, i.e. the content at which contact between nanoinclusions statistically occurs. At a filler content below this latter value, R_{ck} is governed by contacts between the filler and the matrix, while at a filler content above it, contacts between the nanofillers become predominant [20,22]. At the percolation threshold, the value of the overall thermal interface resistance is expected to change as a function of the filler content, leading to a variation in the slope of the thermal conductivity enhancement. The percolation threshold was assumed as the inverse of the AR, as suggested by Shenogina et al. [53]. In order to include the above interfacial phenomena in our thermal analysis, we adopted the modified thermal conductivity model proposed by Chu et al. [25] for nanoinclusions:

$$\lambda_x = \frac{\lambda_{filler}}{2R_{ck}\lambda_{filler}/D + 1}, \tag{1}$$

$$\lambda_z = \frac{\lambda_{filler}}{2R_{ck}\lambda_{filler}/l + 1}, \tag{2}$$

being λ_x and λ_z the modified thermal conductivity in the radial and axial direction of the filler, R_{ck} the overall thermal interface resistance, λ_{filler}, D and l the nominal thermal conductivity, the lateral size and the thickness of the nanofiller, respectively. These modified thermal conductivities were then employed in MF theory calculations to perform an analysis of the thermal conductivity enhancement as a function of the nanofiller content (0%–15% in weight content). In these calculations, the variation of the thermal interface resistances as a function of the filler content was taken into account by the percolation model of Digimat-MF as

$$\frac{\lambda_{eff}}{\lambda_{matrix}} \approx \left(\frac{V - \frac{1}{AR}}{1 - \frac{1}{AR}}\right)^p \quad for \quad V \geq \frac{1}{AR}, \tag{3}$$

being λ_{eff} and λ_{matrix} the PCM nanocomposite and matrix thermal conductivities respectively, V the volume fraction content of the nanoinclusions, and p a characteristic exponent which accounts for the variation of the thermal interface resistance. In our case, the exponent p was determined upon comparisons between MF theory calculations and the experimental measurements previously computed.

In Fig. 9, a schematic representation of the various step performed to obtain the effective thermal conductivity is reported.

3.2. Plant analysis

The PT15+GNP25 (in the range of filler weight content 0%–15%), being the best performing nanocomposite, was envisioned to be used in the shell & tube tank, connected to a daily domestic user and aimed at the storage of cooling energy (Fig. 4).

The numerical analysis of the LHTES system was performed to determine if the charging and discharging processes of the PCM nanocomposites occurred completely for the considered application; this condition, indeed, remarkably influences the PCM storage density [8].

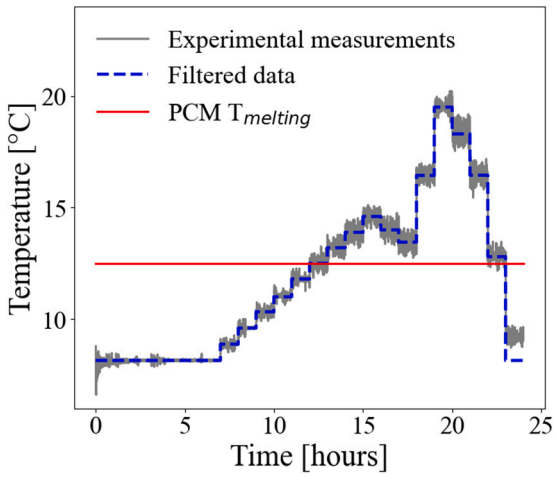

Fig. 10. Daily variation of $T_{tank,in}$ experimentally measured (gray lines) and its hourly averaged value (dashed blue lines). The temperature at the 24th hour was imposed at 8 °C to obtain the daily periodicity of the profile.

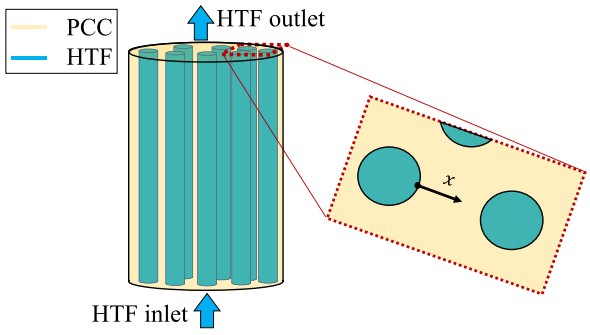

Fig. 11. Schematic representation of the shell and tube tank. x is the direction of the propagation front. PCC is the phase change material nanocomposite, HTF is the heat transfer fluid within the tubes.

Therefore, the output of the analysis was the definition of two nanofiller contents: the minimum filler content – when present –, i.e. the filler content at which the complete solidification (or complete melting) occurs during the discharging (charging) process, and the optimal filler content, at which a trade-off (in the Pareto sense) between specific energy and specific power can be found.

The input data for this analysis were $T_{tank,in}$ (shown in Fig. 10), $\dot{m}_{HTF}$ (~ 0.0750 kg/s), which were measured at the inlet of the tank, and the effective thermal properties of the PCM nanocomposite as a function of the nanofiller content, i.e. the thermal conductivity λ_{eff}, the latent heat L_{eff}, the density ρ_{eff}, and the specific heat capacity $c_{p_{eff}}$. The values of the effective thermal conductivity of the liquid and solid phases of the PCM+GNP25 nanocomposite were obtained by the previously performed MF theory calculations. Contrarily, the other effective properties were computed as weighted averages between those of the pure PCM and of the nanofillers [54]. $T_{tank,in}$, shown in Fig. 10, was obtained by fixing $T_{chiller,out}$ to 7 °C, and by applying the cooling load shown in Fig. 5 via the heat exchanger shown in Fig. 4.

A simplified schematic of the analyzed tank is shown in Fig. 11. In order to determine whether a complete phase change occurs during a daily cycle or not, an analysis of the solidification (melting) propagation front during the charging (discharging) process was carried out. It is worth noting that, in the considered application, the solidification process is expected to be a slower process as compared to that of melting; therefore, it represents the most critical phenomenon. Clearly, a proper operating condition of the storage tank is obtained if, within the entire system, a complete phase transition can be accomplished. This latter condition is fulfilled if, in the configuration shown in Fig. 11, the phase-change front $s(t)$ reaches half of the largest center-to-center distance between two neighboring tubes during the available time for the charging and discharging processes. For the sake of computational simplicity, in this study, we describe the transient phase-change phenomenon of the PCM between two contiguous tubes by means of a one-dimensional analysis along the unique radial direction of a generic tube, namely the x direction shown in Fig. 11.

The analysis of the propagation front for the PCM nanocomposites was carried out considering the simplified Stefan approach: only heat diffusion is taken into account, while convective phenomena are neglected in the phase transition dynamics. Under these assumptions, an analytical solution for a one-dimensional geometry can be obtained [30]. Since the PCM matrix is typically a non-pure substance, the phase transition occurs in a temperature range [30]. In our model, T_m was considered as the mean temperature of the phase transition range (12.5 °C), which is lower than the nominal melting temperature reported by the datasheet of the producer (15 °C). For the solidification process, the following boundary and initial conditions were imposed. The PCM nanocomposite was considered at a homogeneous temperature, T_i, initially greater than that of solidification. Then, at the instant t_0, the temperature at $x = 0$ was imposed equal to $T_{tank,in}$ (at the inlet section). Successively, the latter boundary condition was changed according to the hourly variation of the heat transfer fluid temperature, which follows the profile of $T_{tank,in}$ (see Fig. 10). Under these hypotheses, the temperatures of the PCM nanocomposite in the solid T_s and liquid T_l phases are governed by the diffusion equation [30] as follows:

$$\begin{cases} \frac{\partial^2 T_s(x,t)}{\partial x^2} = \frac{1}{\alpha_s}\frac{\partial T_s(x,t)}{\partial t} & \text{if } 0 < x < s(t) \\ \frac{\partial^2 T_l(x,t)}{\partial x^2} = \frac{1}{\alpha_l}\frac{\partial T_l(x,t)}{\partial t} & \text{if } x > s(t) \end{cases}$$

where the subscripts s and l refer to the solid and liquid phases, respectively. λ is the effective thermal diffusivity, defined as $\alpha = \lambda/\rho c_p$. Energy conservation is imposed at the interface position $x = s(t)$ for $t > 0$, namely

$$\lambda_l \frac{\partial T_l}{\partial x} + \rho L \frac{ds(t)}{dt} = \lambda_s \frac{\partial T_s}{\partial x}, \tag{4}$$

being λ_s and λ_l the effective thermal conductivities of the solid and liquid phases, ρ the effective density (i.e. the weighted average density between the solid and liquid phases) and L the effective specific latent heat. At the solid–liquid interface, the continuity of the temperature field was also imposed, namely: $T_s(s,t) = T_l(s,t) = T_m$. The position of the interface as a function of time was computed by the Neumann solution to the Stefan problem [30] as

$$s(t) = 2 \cdot k \cdot \sqrt{\alpha_s \cdot t}, \tag{5}$$

where k fulfills the following equation:

$$\frac{e^{-k^2}}{erf(k)} + \frac{\lambda_l}{\lambda_s}\sqrt{\frac{\alpha_s}{\alpha_l}}\frac{T_m - T_i}{T_m - T_{tank,in}}\frac{e^{-k^2\cdot\frac{\alpha_s}{\alpha_l}}}{erfc(k\frac{\alpha_s}{\alpha_l})} = \frac{k\pi}{Ste_s}. \tag{6}$$

In Eq. (6), Ste_s is the Stefan number of the solid phase, defined as $Ste_s = C_s(T_m - T_{tank,in})/L$, where C_s is the specific heat capacity of the PCM nanocomposite. Following the same procedure for the liquid phase of the PCM nanocomposite, it is possible to obtain

$$\frac{e^{-k^2}}{erf(k)} + \frac{\lambda_s}{\lambda_l}\sqrt{\frac{\alpha_l}{\alpha_s}}\frac{T_m - T_i}{T_m - T_{tank,in}}\frac{e^{-k^2\cdot\frac{\alpha_l}{\alpha_s}}}{erfc(k\frac{\alpha_l}{\alpha_s})} = \frac{k\pi}{Ste_l} \tag{7}$$

$$s(t) = 2 \cdot k \cdot \sqrt{\alpha_l \cdot t} \tag{8}$$

The adopted Stefan solution is based on a Dirichlet boundary condition for the temperature at $x = 0$, constant in time, which differs from our layout in that the temperature of the heat transfer fluid varies on an hourly basis. Therefore, an approximated procedure was adopted to take into account the variation of the temperature of the Dirichlet

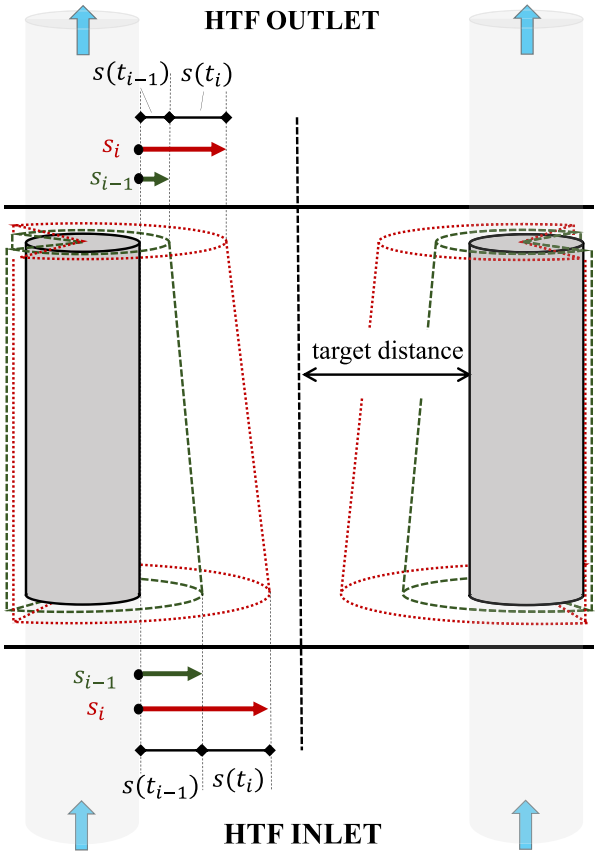

Fig. 12. Schematic representation of a portion of two adjacent tubes of the shell & tube tank. In the left tube, the figures of merit considered in the analytical model are depicted.

condition at $x = 0$. The contribution of the ith hour to the overall distance covered by the propagation front ($s(t_i)$) has been obtained by considering the layer of the material solidified (or melted) during the previous $(i-1)$-th hours. Therefore, this contribution was computed as

$$s(t_i) = s_i - s_{i-1} = 2k_i\sqrt{\alpha_i(3600 \cdot i)} - \sum_{j=1}^{t-1} s(t_j), \tag{9}$$

being s_i the phase change front obtained by applying the boundary condition of the ith hour to all the hours up to i; s_{i-1} is the propagation front already reached in the previous $i-1$ hours. Finally, the total propagation front of the phase transition was computed by summing up the contributions, $s(t_i)$, at each hour. This procedure is schematically shown in Fig. 12, in which, for the sake of simplicity, only the first two hours are displayed. More in detail, the dashed lines of Fig. 12 show the three-dimensional phase transition front at the i and the $(i-1)$ hours. The red arrows show the computed propagation front of the i-hours obtained by applying the boundary conditions of the i-hour to all the hours up to i, i.e. s_i. On the other hand, the green arrows show the propagation front obtained with the boundary conditions of the $(i-1)$-hour. Finally, $s(t_i)$ is the contribution of the i-hour to the total propagation front.

In addition to the inlet section, the above model was employed also at the outlet section of the tubes, where the less favorable conditions for complete melting/freezing within the tank are expected. Due to the heat transfer along the storage tank, we indeed expect the local Stefan number to be lower at the outlet, as compared to the one at the inlet. Then, at the outlet section, a slower propagation front is expected. This concept has been schematically depicted by the conical shape of the

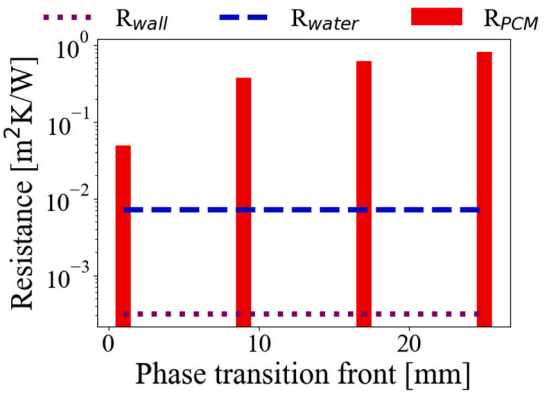

Fig. 13. Thermal resistances as a function of the solidification front in the PCM nanocomposite: convective resistance of the heat transfer fluid (dashed blue line), conductive resistance of the wall (dashed purple line) and conductive resistance of the PCM nanocomposite (red bars).

phase transition fronts, i.e. the green and red dashed lines in Fig. 12. $T_{tank,out}$ can be obtained by means of the ϵ-NTU method [55,56]. At each hour, the total thermal resistance of the heat transfer depends on the convective resistance at the tube/fluid interface R_{water}, the conductive resistance of the wall R_{wall}, and the hourly average conductive resistance of the layer of PCM nanocomposite R_{PCM}. As the computation of the NTU coefficient depends on the total thermal resistance, and being the latter the output of the analysis, the method was performed iteratively, up to convergence. In the laminar region, the convective heat transfer resistance at the fluid/tube interface was obtained as [55]

$$h_f = \frac{Nu\lambda_{HTF}}{2r_i}, \tag{10}$$

$$Nu = 3.66 + \frac{0.0668\frac{2r_i}{H} \cdot Re \cdot Pr}{1 + 0.004(\frac{2r_i}{H} Re \cdot Pr)^{2/3}}, \tag{11}$$

where Nu is the Nusselt number, λ_{HTF} the thermal conductivity of the heat transfer fluid, r_i and H the internal radii and the height of the tube, Re the Reynolds number, and Pr the Prandtl number. The analysis of the three main thermal resistances as a function of the front position in Fig. 13 shows that the resistance due to the layer of PCM, starting from a thickness of a few millimeters, is the dominant one as it is at least one order of magnitude larger than the others.

Finally, the results obtained by adopting the modified Stefan approach have been compared with CFD simulations obtained by means of COMSOL. Here, the coupling between the laminar fluid flow of the HTF and the heat transfer in the HTF and the PCM (modeled as a solid) was exploited, and a two-dimensional axial-symmetric geometry considered (a single tube, following the same layout of the Stefan approach shown in Fig. 12). The laminar flow module was chosen for the HTF as the Reynolds number within a single tube was equal to 90, being the diameter equal to 16 mm, $\dot{m}_{tube} = \dot{m}_{HTF}/N_{tubes} = 0.01136$ kg/s, and the HTF demineralized water. A mapped mesh was developed and the adaptive mesh refinement settings of COMSOL were used, thus resulting in 12 mesh refinements, from 52272 to 112714 elements.

4. Results and discussion

4.1. Material analysis results

Experimental thermal conductivity measurements of the three PCM nanocomposites (PCM+GNP25, PCM+GNP15 and PCM+GNP5) were performed both for the liquid and solid phase, with a nanofiller content of up to 3.53% in weight content. In the liquid phase, the thermal

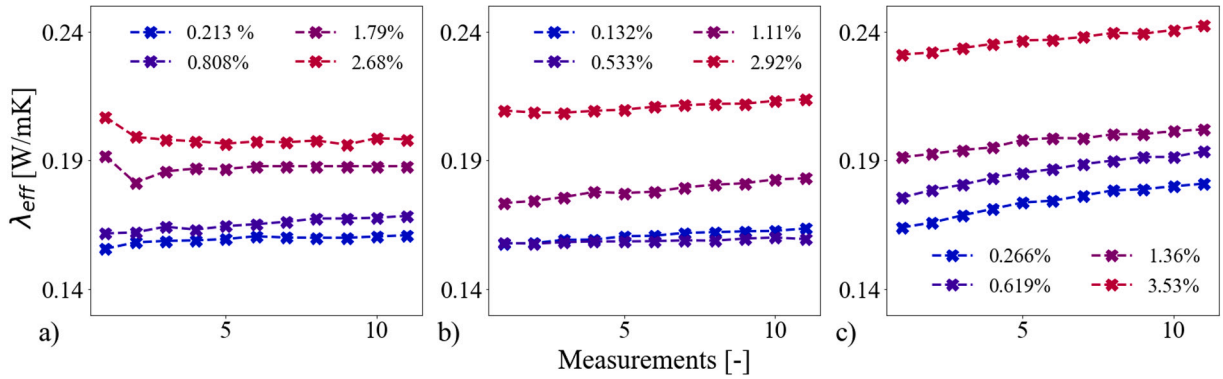

Fig. 14. Comparison between the precipitation of the samples additivated with various weight contents of (a) GNP5 (b) GNP15 and (c) and GNP25. Dashed lines are guides for the eye.

conductivity measurement of the well-dispersed PCM nanocomposite sample was done within two hours after the mechanical mixing, noticing a not significant precipitation, as shown in Fig. 14. In fact, among the three PCM nanocomposites, the maximum difference between the outcome of the first measurement and the average value from the twelve tested samples was 6.02%. Nevertheless, the first value of each measurement was considered to neglect the precipitation impact on the effective thermal conductivity. The increase in thermal conductivity caused by the precipitation of nanofillers was due to the specific layout of the sensor, which measures the thermal conductivity of the portion of material close to the sensor, i.e. in the bottom part of the sample (see Fig. 2). Therefore, due to nanofiller precipitation, the portion of the sample in contact with the sensor has a greater local concentration of the filler, which leads to a higher thermal conductivity detected by the sensor. Nanofillers with a greater volume (GNP25) precipitated more evidently, because of their higher weight, as can be identified in Fig. 14 (c). Instead, a more relevant precipitation of nanofillers was typically observed later, especially in the medium (~ dozen hours) and long (~ several days) term. In fact, measurements with PT15+3.53% in weight content of GNP25, PT15+2.92% of GNP15 and PT15+2.68% of GNP5 were performed a few days after the mixing process (from 1 to 3 days), showing almost complete precipitation of the nanofiller. From this analysis, it can be concluded that PCM nanocomposites produced solely by mechanical mixing become unstable after a few hours. However, for our purposes, these conditions were considered sufficient, as the preparation of medium (or long) term-stable PCM nanocomposites goes beyond the scope of the present work.

In Fig. 15, a comparison between the thermal conductivities of the liquid phases of the three PCM nanocomposites is reported. It is found that the best performing filler is the GNP25, for which the effective thermal conductivity reaches a maximum enhancement of 54% at a nanofiller weight content of 3.53%. Such remarkable result can be possibly attributed to the high AR, as also reported by Yang et al. [51].

The experimental measurements were compared with the FE simulations to estimate the thermal interface resistance values. The comparison between the numerical simulation performed with different thermal interface resistances and the experimental measurements is shown in Fig. 16. The thermal interface resistances values vary from 3e−7 Km^2/W to almost 3e−6 Km^2/W for the three nanocomposites. These values are higher than the thermal interface resistances values reported by theoretical studies and obtained by means of molecular dynamics simulations [19]. Molecular dynamics simulations, in fact, take into account solely the local phonon scattering at the interfaces, thus neglecting the imperfect contact between surfaces [24]. At the meso- and macroscale, the latter term is the main contribution to the overall thermal interface resistances. It is worth noting that the adhesion between nanofillers and PCM matrix could be enhanced by

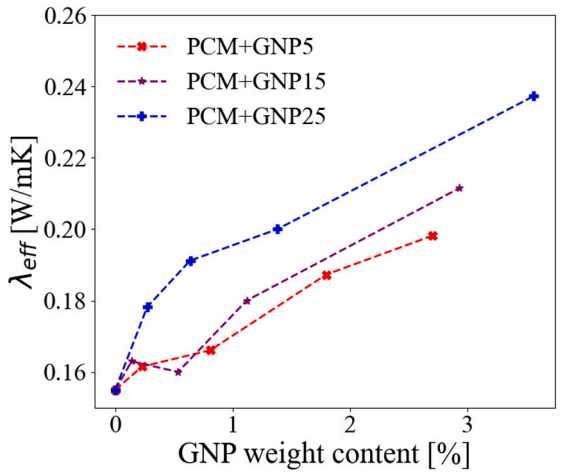

Fig. 15. Comparison of the impact of the three nanofillers on the effective thermal conductivities of PCM samples in liquid phases as a function of different weight contents. Dashed lines are guides for the eye.

applying a pressure to the sample, as the thermal interface resistances depend on pressure [24].

In the samples additivated with GNP5 and GNP15, the effective thermal conductivities experimentally measured were found to be best-fitted by a linear regression (with a R-squared of 0.985 for GNP5 and 0.969 for GNP15), thus resulting in an almost constant thermal interface resistance, as shown in Fig. 16. On the other hand, a remarkable variation of the best matching thermal interface resistance value as a function of the filler content is visible for the PCM+GNP25 sample. In fact, the addition of GNP25 caused a significant thermal conductivity enhancement for nanofiller content up to 1% in weight. In particular, at 0.619% of GNP25 the thermal conductivity enhancement ($\eta = \lambda_{eff}/\lambda_{matrix}$) was 1.23, while at 3.53% it reached 1.54. Hence, the nanofiller content increase from 0.619 to 3.53% caused an enhancement similar to that produced by a GNP content up to 0.619%. This sudden variation of the impact of GNP25 could be attributed to the contacts between nanofillers, which statistically occur at the percolation threshold [22]. In this specific case, the further contacts between nanofillers increased the thermal interface resistances. This was attributed to the mixing procedures: by exploiting only mechanical mixing and by not applying a pressure on the nanocomposite, a weak adhesion between the components of the sample was obtained. Similar increases in the thermal interface resistance were obtained in the literature [57–59]. Contrarily, the additivation performed with nanocomposites with a smaller lateral size (GNP5 and GNP15) produces gradual enhancements to the continuity of the thermal path within

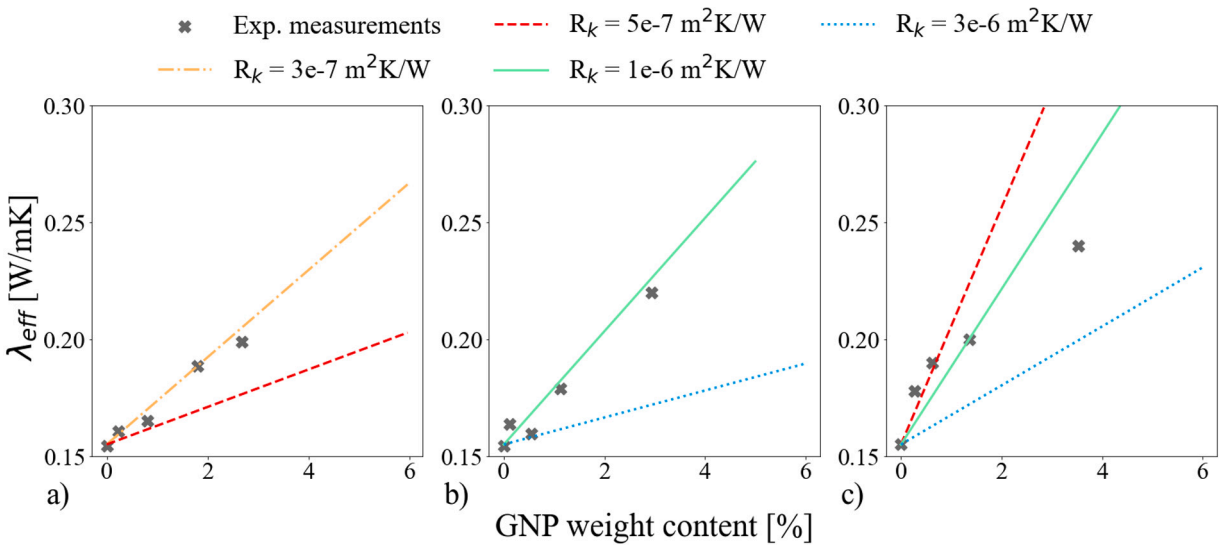

Fig. 16. Comparison between the thermal interface resistances of liquid phases of (a) PT15+GNP5 (b) PT15+GNP15 and (c) PT15+GNP25 obtained by the synergistic approach between the experimental measurements (gray crosses) and the finite element simulations (lines).

the material [60], thus leading to a modest variation of the thermal interface resistances as a function of the nanofiller content.

It is worth noting that the trends of the experimental thermal conductivity enhancements and the thermal interface resistances of the different PCM nanocomposites seem to be in apparent contrast: the enhancement in the thermal conductivity presented the opposite trend to that of the thermal interface resistances value. The thermal interface resistances of PT15+GNP15 and PT15+GNP5 are lower than that of PT15+GNP25 (R_{ck} = 7e−7 ÷ 5e−6 Km^2/W). However, the enhancement due to GNP25 is greater than that generated by GNP5 and GNP15. This phenomenon is due to the definition of thermal interface resistance: by representing the measure of the resistance of an interface to a thermal flux, its value is directly proportional to the contact area of the two materials, i.e. the total surface area of the nanofiller. At a fixed weight content, however, nanofillers with smaller AR have a lower total surface area, thus leading to apparent lower thermal interface resistances.

Finally, these observed overall values of the thermal interface resistances were introduced in the Digimat-MF module to extrapolate the effective thermal conductivity of different nanocomposites with filler content up to 15% in weight. The exponent p of Eq. (3), which defines the variation of thermal interface resistance as a function of the nanofiller content, was obtained by best-fitting the MF theory calculations with the experimental measurements. The resulting p values obtained for the model for PCM+GNP25, PCM+GNP15 and PCM+GNP5 were 0.67, 0.86 and 0.87, respectively. These results confirm the increase of the linearity trend of the effective thermal conductivity as a function of the GNP content caused by the decrease of the nanofiller lateral size, at least in the content range experimentally tested. A possible limitation of this approach could be attributed to the fact that, in the MF theory calculations, the interfacial thermal resistance variation experimentally measured (and implemented in the model through the exponent p) was imposed also outside the nanofiller range experimentally measured (> 3.53%). Therefore, considering nanofillers with lower AR, the model is not able to predict the possible change in the slope of the curve, as it is due to the percolation which occurs outside the filler content experimentally measured. However, nanofillers with lower ARs cause a gradual increase in the continuity of the thermal path due to their reduced sizes. In such cases, therefore, the change in the slope is expected to be more modest. Finally, this limitation is negligible when analyzing nanofillers with noticeable AR, as percolation occurs at a lower filler content.

4.2. Plant analysis results

During the discharging process, the phase change propagation front of the non-additivated PCM reached 75.6% and 61.2% of the target distance at the inlet and outlet section of the tube, respectively, leading to a partial solidification of the material. During the charging process, similar results were obtained, as the propagation front reached 75.2% and 62.8% of the target distance at the inlet and outlet sections, respectively. Hence, if the bulk PCM was used in the considered application, complete phase transitions would not occur inside the shell & tube tank.

The addition of GNP25 within the PCM, as shown in Section 4.1, thanks to its remarkable thermal conductivity enhancement, yields an increase in the heat conduction of the material. Such an increase is desirable to obtain faster propagation fronts during the charging and discharging processes. Evidence of this is presented in Figs. 17 (a) and (b), where the solidification fronts are depicted as a function of the GNP25 content at the inlet and outlet sections, respectively. Nevertheless, while at the inlet section the target distance was reached for weight contents of GNP25 equal to or higher than 3.06% (black bar in Fig. 17), at the outlet section the propagation front of the PCM nanocomposites was always smaller than the target distance (at least up to 15% of GNP25). A similar trend was obtained also in the melting process. Notably, the increase in the propagation front as a function of the GNP25 content in the outlet section is moderate, as can be observed by comparison of Figs. 17 (a) and (b). In fact, the enhanced heat conduction leads to a larger heat power exchanged between the heat transfer fluid and the PCM along the length of the tube, thus resulting in a higher temperature of the heat transfer fluid at the outlet section. Therefore, an even more detrimental boundary condition for the propagation front was present at the outlet section of the tank containing the PCM nanocomposite.

A comparison between the analytical approach and CFD simulations in the case of the solidification of the bulk PCM was carried out to verify the model proposed in our work. The propagation of the front at the end of the solidification process simulated by COMSOL was 14% lower at the inlet section and 33% at the outlet section. The difference was mainly attributed to the fact that, in the Stefan approach, the temperature of the HTF in the radial direction is considered constant, and a greater temperature gradient at the interface is present.

Finally, a Pareto-based analysis of the PCM+GNP25 nanocomposite was carried out to define the optimal nanofiller content as the best compromise between specific power and specific energy. In Figs. 18 (a) and (b), the optimal nanofiller weight contents at the inlet and outlet

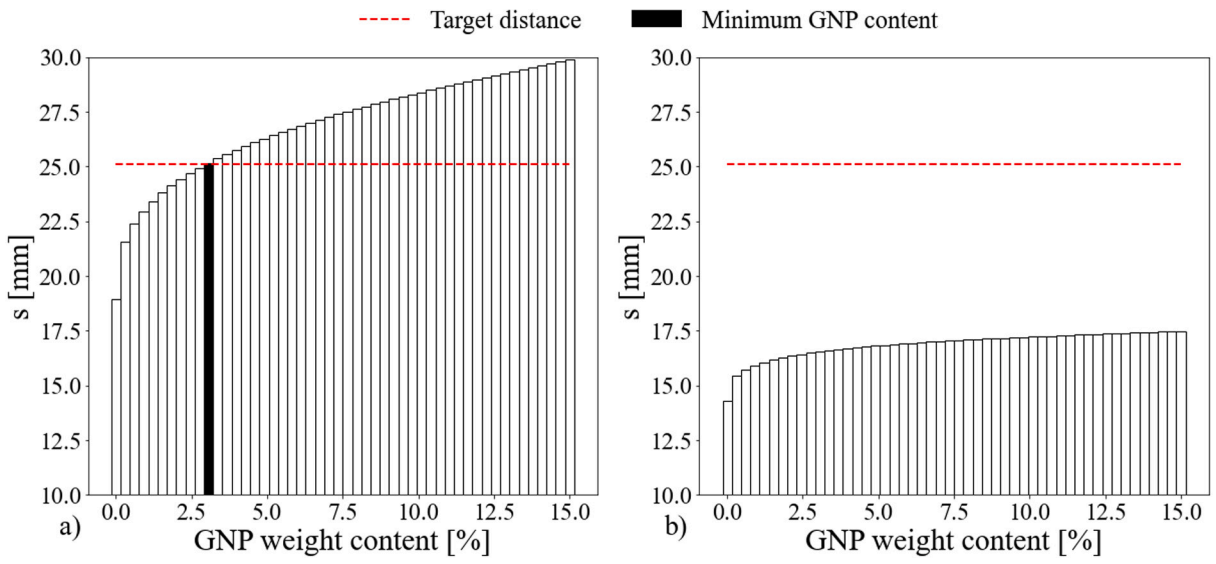

Fig. 17. Propagation of the solidification front of PCM+GNP25 as a function of the nanofiller content (a) at the inlet and (b) outlet sections.

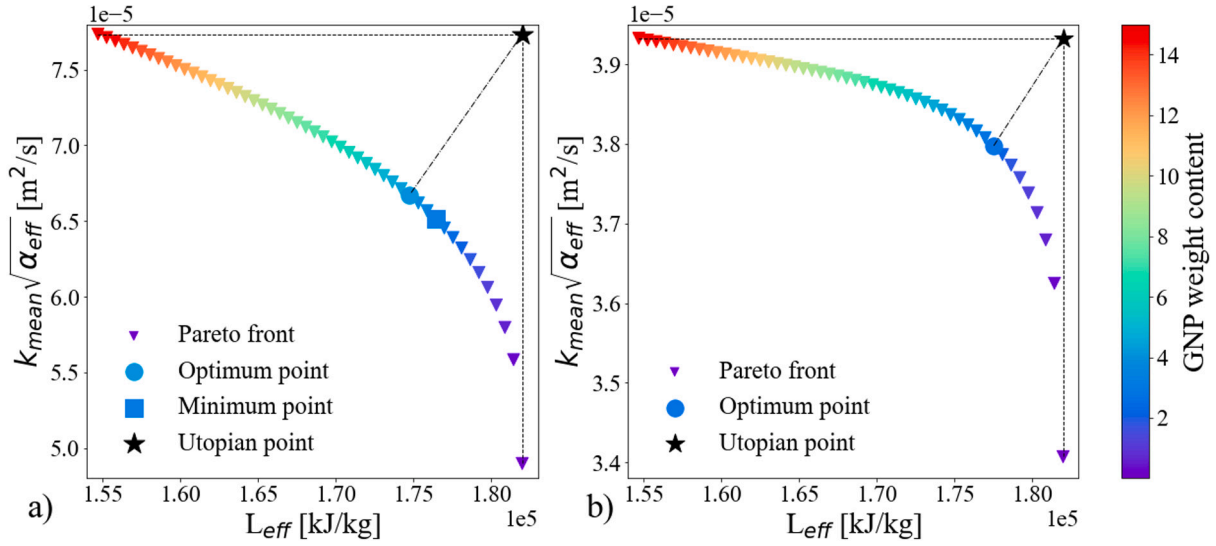

Fig. 18. Pareto analysis with respect to the specific power and specific energy at the (a) inlet and (b) outlet sections. The x-axis represents the specific energy and the y-axis is linked to the specific power of the PCM nanocomposite.

sections that were obtained by considering the solidification process are shown. The effective latent heat L_{eff} is linked to the specific energy as it represents the amount of latent thermal energy that can be stored within the material. On the other hand, $k_{mean}\sqrt{\alpha_{eff}}$, which is related to the rate of the charging and discharging processes as shown in Eq. (5), is connected to the specific power. k_{mean} indicates the average value of k (for each nanofiller content considered) over the discharging hours, as it varies according to the boundary conditions, i.e. the temperature of the heat transfer fluid. Among the different criteria for finding optimum attainable points among a Pareto front, the utopia point criterion was chosen for the definition of the optimum nanofiller content. According to this criterion, the optimum point is the closest one – normalized with respect to the minimum and maximum values of the specific energy and power – to the utopia point. In our case, the utopia point would be obtained by the increase in the specific power without the decrease in specific energy [61]. According to this analysis, therefore, the considered PCM nanocomposite should be used with a GNP weight content in the range of 2.45-3.98% (the optimum nanofiller content at the outlet and inlet sections, respectively), to obtain a suitable compromise between the increase in the specific power and the decrease in the specific energy.

5. Conclusions

In this study, a multi-scale analysis was performed to assess the impact of nanofillers addition on the thermal behavior of a PCM matrix. At the material scale, the two main purposes of the work were: (i) the estimate of the interfacial thermal resistances of the three PCM nanocomposites as a function of the nanofiller content, which was obtained by comparing finite element simulations and experimental measurements; (ii) the prediction of the effective thermal conductivity of the PCM nanocomposite in a wider nanofiller content range than that experimentally measured. At the plant scale, a new fast procedure for the thermal design of a lab-scale shell & tube tank containing the PCM nanocomposite was carried out to define the optimal nanofiller contents. This analysis was performed by following an approximated procedure based on an analytical solution to the Stefan problem. This procedure has been also compared with CFD simulations, obtaining acceptable discrepancies. The results of these analysis suggest that the

addition of highly conductive nanofillers requires an optimal design of the storage system, as it does not necessarily lead to the expected specific energy and power enhancement. Moreover, the thermal conductivity measurements that were performed in the medium term have indicated the unavoidable precipitation of nanofillers in PCM nanocomposites produced solely by mechanical mixing. Therefore, further research needs to be performed to develop a storage system with sufficiently high thermal conductivity and latent heat, which does not suffer from precipitation at the same time. In this respect, and in perspective, solid-to-solid PCMs (SS-PCMs) have recently gained attention, as they absorb and release the latent heat via phase transitions between two solid phases (crystalline, semicrystalline, or amorphous). The addition of highly conductive nanofillers within such materials could increase the thermal conductivity in the absence of phase segregation.

Declaration of competing interest

The authors declare that they have no known competing financial interests or personal relationships that could have appeared to influence the work reported in this paper.

Data availability

Data will be made available on request

Acknowledgments

A.R. and E.C. acknowledge the financial support of the research contract PTR 2019/21 ENEA (Sviluppo di modelli per la caratterizzazione delle proprietà di scambio termico di PCM in presenza di additivi per il miglioramento dello scambio termico) funded by the Italian Ministry of Economic Development (MiSE).

References

[1] AD International Renewable Energy Agency, Innovation Outlook: Thermal Energy Storage, IRENA, 2020.
[2] C. Zhang, Y. Qiu, J. Chen, Y. Li, Z. Liu, Y. Liu, J. Zhang, C.S. Hwa, A comprehensive review of electrochemical hybrid power supply systems and intelligent energy managements for unmanned aerial vehicles in public services, Energy AI 9 (2022) 100175.
[3] P.D. Angelis, M. Tuninetti, L. Bergamasco, L. Calianno, P. Asinari, F. Laio, M. Fasano, Data-driven appraisal of renewable energy potentials for sustainable freshwater production in africa, Renew. Sustain. Energy Rev. 149 (2021) 111414.
[4] G. Alva, Y. Lin, G. Fang, An overview of thermal energy storage systems, Energy 144 (2018) 341–378.
[5] M. Fasano, L. Bergamasco, A. Lombardo, M. Zanini, E. Chiavazzo, P. Asinari, Water/ethanol and 13x zeolite pairs for long-term thermal energy storage at ambient pressure, Front. Energy Res. 7 (2019) 148.
[6] G. Trezza, L. Bergamasco, M. Fasano, E. Chiavazzo, Minimal crystallographic descriptors of sorption properties in hypothetical [MOF]s and role in sequential learning optimization, Npj Comput. Mater. 8 (2022) 1–14.
[7] I. Sarani, B. Xie, Z. Bao, W. Huo, X. Li, Y. Xu, B. Wang, K. Jiao, Analysis of phase change material thermal effects in large-scale proton-exchange membrane fuel cell based on open-source computational fluid dynamics, Appl. Therm. Eng. 216 (2022) 119143.
[8] M. Neri, E. Chiavazzo, L. Mongibello, Numerical simulation and validation of commercial hot water tanks integrated with phase change material-based storage units, J. Energy Storage 32 (2020) 101938.
[9] Y. Lin, Y. Jia, G. Alva, G. Fang, Review on thermal conductivity enhancement, thermal properties and applications of phase change materials in thermal energy storage, Renew. Sustain. Energy Rev. 82 (2018) 2730–2742.
[10] T. Xiong, K.W. Shah, Chapter 26 - nanomaterials for enhancement of thermal energy storage in building applications, in: C. Mustansar Hussain (Ed.), Handbook of Functionalized Nanomaterials for Industrial Applications, Micro and Nano Technologies, Elsevier, 2020, pp. 829–864.
[11] Y. Zhao, X. Min, Z. Huang, Y. Liu, X. Wu, M. Fang, Honeycomb-like structured biological porous carbon encapsulating PEG: A shape-stable phase change material with enhanced thermal conductivity for thermal energy storage, Energy Build. 158 (2018) 1049–1062.
[12] X. Min, M. Fang, Z. Huang, Y. Liu, Y. Huang, R. Wen, T. Qian, X. Wu, Enhanced thermal properties of novel shape-stabilized PEG composite phase change materials with radial mesoporous silica sphere for thermal energy storage, Sci. Rep. 5 (2015) 12964.
[13] Y. Zhao, B. Sun, P. Du, X. Min, Z. Huang, Y. Liu, X. Wu, M. Fang, Hierarchically channel-guided porous wood-derived shape-stabilized thermal regulated materials with enhanced thermal conductivity for thermal energy storage, Mater. Res. Express 6 (2019) 115515.
[14] F. Cheng, X. Zhang, R. Wen, Z. Huang, M. Fang, Y. Liu, X. Wu, X. Min, Thermal conductivity enhancement of form-stable tetradecanol/expanded perlite composite phase change materials by adding CU powder and carbon fiber for thermal energy storage, Appl. Therm. Eng. 156 (2019) 653–659.
[15] X. Li, Y. Zhao, X. Min, J. Xiao, X. Wu, R. Mi, Y. Liu, Z. Huang, M. Fang, Carbon nanotubes modified graphene hybrid aerogel-based composite phase change materials for efficient thermal storage, Energy Build. 273 (2022) 112384.
[16] L.-W. Fan, X. Fang, X. Wang, Y. Zeng, Y.-Q. Xiao, Z.-T. Yu, X. Xu, Y.-C. Hu, K.-F. Cen, Effects of various carbon nanofillers on the thermal conductivity and energy storage properties of paraffin-based nanocomposite phase change materials, Appl. Energy 110 (2013) 163–172.
[17] R. Srivastava, M. Fasano, S.M. Nejad, H.C. Thielemann, E. Chiavazzo, P. Asinari, Modeling carbon-based smart materials, in: C. Charitidis, E. Koumoulos, D. Dragatogiannis (Eds.), Carbon-Based Smart Materials, 2020, pp. 33–79.
[18] S.M. Nejad, R. Srivastava, F.M. Bellussi, H.C. Thielemann, P. Asinari, M. Fasano, Nanoscale thermal properties of carbon nanotubes/epoxy composites by atomistic simulations, Int. J. Therm. Sci. 159 (2021) 106588.
[19] M. Fasano, M.B. Bigdeli, M.R.V. Sereshk, E. Chiavazzo, P. Asinari, Thermal transmittance of carbon nanotube networks: Guidelines for novel thermal storage systems and polymeric material of thermal interest, Renew. Sustain. Energy Rev. 41 (2015) 1028–1036.
[20] E. Chiavazzo, P. Asinari, Reconstruction and modeling of 3D percolation networks of carbon fillers in a polymer matrix, Int. J. Therm. Sci. 49 (2010) 2272–2281.
[21] S. Mohamma Nejad, M. Bozor Bigdeli, R. Srivastava, M. Fasano, Heat transfer at the interface of graphene nanoribbons with different relative orientations and gaps, Energies 12 (2019) 796.
[22] R.J. Warzoha, A.S. Fleischer, Effect of graphene layer thickness and mechanical compliance on interfacial heat flow and thermal conduction in solid–liquid phase change materials, ACS Appl. Mater. Interfaces 6 (2014) 12868–12876, PMID: 24983698.
[23] L. Bergamasco, M. Alberghini, M. Fasano, A. Cardellini, E. Chiavazzo, P. Asinari, Mesoscopic moment equations for heat conduction: Characteristic features and slow–fast mode decomposition, Entropy 20 (2018) 126.
[24] B.N.J. Persson, Thermal interface resistance: Cross-over from nanoscale to macroscale, J. Phys.: Condens. Matter 26 (2013) 015009.
[25] K. Chu, C.-c. Jia, W.-s. Li, Effective thermal conductivity of graphene-based composites, Appl. Phys. Lett. 101 (2012) 121916.
[26] Z. Xu, S. He, J. Zhang, S. Huang, A. Chen, X. Fu, P. Zhang, Relationship between the structure and thermal properties of polypropylene/graphene nanoplatelets composites for different platelet-sizes, Compos. Sci. Technol. 183 (2019) 107826.
[27] R.P. Singh, J.Y. Sze, S.C. Kaushik, D. Rakshit, A. Romagnoli, Thermal performance enhancement of eutectic PCM laden with functionalised graphene nanoplatelets for an efficient solar absorption cooling storage system, J. Energy Storage 33 (2021) 102092.
[28] G. He, X. Tian, Y. Dai, X. Li, C. Lin, Z. Yang, S. Liu, Bioinspired interfacial engineering of polymer based energetic composites towards superior thermal conductivity via reducing thermal resistance, Appl. Surf Sci. 493 (2019) 679–690.
[29] L. Entropy Solutions, Puretemp 15 technical information, 2017, https://www.puretemp.com.
[30] D.W. Hahn, M.N. Ozisik, Heat Conduction, John Wiley & Sons, 1993.
[31] E. Paroutoglou, P. Fojan, L. Gurevich, G. Hultmark, A. Afshari, Thermal analysis of organic and nanoencapsulated electrospun phase change materials, Energies 14 (2021).
[32] V. Kumaresan, R. Velraj, S.K. Das, The effect of carbon nanotubes in enhancing the thermal transport properties of PCM during solidification, Heat Mass Transf. 48 (2012) 1345–1355.
[33] L.-W. Fan, X. Fang, X. Wang, Y. Zeng, Y.-Q. Xiao, Z.-T. Yu, X. Xu, Y.-C. Hu, K.-F. Cen, Effects of various carbon nanofillers on the thermal conductivity and energy storage properties of paraffin-based nanocomposite phase change materials, Appl. Energy 110 (2013) 163–172.
[34] M. Sangermano, L. Calvara, E. Chiavazzo, L. Ventola, P. Asinari, V. Mittal, R. Rizzoli, L. Ortolani, V. Morandi, Enhancement of electrical and thermal conductivity of SU-8 photocrosslinked coatings containing graphene, Prog. Org. Coat. 86 (2015) 143–146.
[35] A. Ribezzo, G. Falciani, L. Bergamasco, M. Fasano, E. Chiavazzo, An overview on the use of additives and preparation procedure in phase change materials for thermal energy storage with a focus on long term applications, J. Energy Storage 53 (2022) 105140.
[36] B.M.S. Punniakodi, R. Senthil, Recent developments in nano-enhanced phase change materials for solar thermal storage, Sol. Energy Mater. Sol. Cells 238 (2022) 111629.
[37] E.J. D'Oliveira, S.C.C. Pereira, D. Groulx, U. Azimov, Thermophysical properties of nano-enhanced phase change materials for domestic heating applications, J. Energy Storage 46 (2022) 103794.

[38] D. Kuvandykova, A New Transient Method to Measure Thermal Conductivity of Asphalt, C-Therm Technologies, 2010.
[39] W. Xiao, X. Zhai, P. Ma, T. Fan, X. Li, Numerical study on the thermal behavior of graphene nanoplatelets/epoxy composites, Results Phys. 9 (2018) 673–679.
[40] L. Mongibello, N. Bianco, M. Caliano, G. Graditi, Comparison between two different operation strategies for a heat-driven residential natural gas-fired CHP system: Heat dumping vs. load partialization, Appl. Energy 184 (2016) 55–67.
[41] J. Guo, Z. Du, G. Liu, X. Yang, M.-J. Li, Compression effect of metal foam on melting phase change in a shell-and-tube unit, Appl. Therm. Eng. 206 (2022) 118124.
[42] S. Riahi, M. Evans, M. Belusko, R. Flewell-Smith, R. Jacob, F. Bruno, Transient thermo-mechanical analysis of a shell and tube latent heat thermal energy storage for CSP plants, Appl. Therm. Eng. 196 (2021) 117327.
[43] S. Riahi, M. Evans, M. Belusko, M. Liu, F. Bruno, Orientation impact on structural integrity of a shell and tube latent heat thermal energy storage system, J. Energy Storage 52 (2022) 104829.
[44] G.S. Sodhi, V. Kumar, P. Muthukumar, Design assessment of a horizontal shell and tube latent heat storage system: Alternative to fin designs, J. Energy Storage 44 (2021) 103282.
[45] M.-J. Li, M.-J. Li, X.-D. Xue, D. Li, Optimization and design criterion of the shell-and-tube thermal energy storage with cascaded PCMs under the constraint of outlet threshold temperature, Renew. Energy 181 (2022) 1371–1385.
[46] e Xstream, Digimat User's Manual, 2020.
[47] T. Mori, K. Tanaka, Average stress in matrix and average elastic energy of materials with misfitting inclusions, Acta Metall. 21 (1973) 571–574.
[48] J.D. Eshelby, R.E. Peierls, The determination of the elastic field of an ellipsoidal inclusion, and related problems, Proc. R. Soc. Lond. Ser. A. 241 (1957) 376–396.
[49] W. Voigt, Ueber die beziehung zwischen den beiden elasticitättsconstanten isotroper körper, Ann. Phys. 274 (1889) 573–587.
[50] S. Depaifve, S. Hermans, D. Ruch, A. Laachachi, Combination of micro-computed X-ray tomography and electronic microscopy to understand the influence of graphene nanoplatelets on the thermal conductivity of epoxy composites, Thermochim. Acta 691 (2020) 178712.
[51] X.S. Yang, L. Zhou, K.Y. Liu, Z.Y. Liu, Q.Z. Wang, B.L. Xiao, Z.Y. Ma, Finite element prediction of the thermal conductivity of GNP/Al composites, Acta Metall. Sinica (Engl. Lett.) 35 (2022) 825–838.
[52] A. Ribezzo, M. Fasano, L. Bergamasco, L. Mongibello, E. Chiavazzo, Multi-scale numerical modelling for predicting thermo-physical properties of phase-change nanocomposites for cooling energy storage, Tecnica Italiana-Italian J. Eng. Sci. 65 (2021) 201–204.
[53] N. Shenogina, S. Shenogin, L. Xue, P. Keblinski, On the lack of thermal percolation in carbon nanotube composites, Appl. Phys. Lett. 87 (2005) 133106.
[54] B. Buonomo, D. Ercole, O. Manca, S. Nardini, Numerical analysis on a latent thermal energy storage system with phase change materials and aluminum foam, Heat Transf. Eng. 41 (2020) 1075–1084.
[55] Heat Exchangers, John Wiley & Sons, Ltd, pp. 797–912.
[56] A. Bologna, M. Fasano, L. Bergamasco, M. Morciano, F. Bersani, P. Asinari, L. Meucci, E. Chiavazzo, Techno-economic analysis of a solar thermal plant for large-scale water pasteurization, Appl. Sci. 10 (2020) 4771.
[57] A. Rybak, Processing Influence on Thermal Conductivity of Polymer Nanocomposites, pp. 463–487.
[58] Y.S. Song, J.R. Youn, Influence of dispersion states of carbon nanotubes on physical properties of epoxy nanocomposites, Carbon 43 (2005) 1378–1385.
[59] F. Shahzad, S. Dildar Haider Naqvi, C.M. Koo, Chapter 5 - Thermal conduction behavior of graphene and graphene–polymer composites, in: G. Zhang (Ed.), Thermal Transport in Carbon-Based Nanomaterials, Micro and Nano Technologies, Elsevier, 2017, pp. 113–134.
[60] Z. Xu, S. He, J. Zhang, S. Huang, A. Chen, X. Fu, P. Zhang, Relationship between the structure and thermal properties of polypropylene/graphene nanoplatelets composites for different platelet-sizes, Compos. Sci. Technol. 183 (2019) 107826.
[61] N. Bianco, M. Iasiello, G.M. Mauro, L. Pagano, Multi-objective optimization of finned metal foam heat sinks: Tradeoff between heat transfer and pressure drop, Appl. Therm. Eng. 182 (2021) 116058.